PCCP

PAPER

Tracer diffusion of ^{96}Zr and ^{134}Ba in polycrystalline $BaZrO_3$

Rokas Sažinas[a, b], Isao Sakaguchi[b], Ida Hasle[c], Jonathan M. Polfus[d], Reidar Haugsrud[c], Mari-Ann Einarsrud[a] and Tor Grande[a]*

Received 00th January 20xx,
Accepted 00th January 20xx

DOI: 10.1039/x0xx00000x

www.rsc.org/

Cation tracer diffusion in polycrystalline cubic $BaZrO_3$ perovskite was studied using the stable isotopes ^{134}Ba and ^{96}Zr in air at 1015-1200 and 1300-1500 °C, respectively. Thin films of ^{134}BaO and $^{96}ZrO_2$ were deposited on polished $BaZrO_3$ pellets by drop casting of aqueous precursor solutions containing the tracers. Isotope distribution profiles were recorded using secondary ion mass spectrometry. All the depth profiles exhibited two distinct regions, which enabled assessment of both lattice and grain boundary diffusion using Fick's second law and Whipple-Le Clair's equation. The grain boundary diffusion of both cations was several orders of magnitude higher than lattice diffusion. Lattice diffusion of Ba^{2+} was found to be significantly faster that lattice diffusion of Zr^{4+}, while the activation energies were comparable, respectively 395±44 and 435±67 kJ/mol. Activation energies for the diffusion of Ba^{2+} and Zr^{4+} through a Ba^{2+} vacancy were calculated by density functional theory using the nudged elastic band method. The calculated and experimental activation energies were in excellent agreement. The cation diffusion data in $BaZrO_3$ is compared to previous data on A and B-site diffusivity in perovskites. Finally, the diffusivity of Zr^{4+} in compounds with perovskite and fluorite structure is discussed in relation to the chemical stability of $BaZrO_3$-based materials.

1 Introduction

$BaZrO_3$ (BZ) based perovskite materials have attracted considerable attention due to their high proton conductivity, with potential applications in protonic ceramic fuel cells (PCFC), electrolyzers, gas sensors, and hydrogen membrane technology.[1-6] The mobility of cations in BZ and related materials has not been studied so far despite the challenges with solid state sintering of BZ materials,[7] a process closely related to cation diffusivity. The poor sinterability and the role of point defects such as cation vacancies, specifically on the A-site of the perovskite, have been debated in particular due to the potential loss of volatile BaO during sintering.[8, 9] Recently, the A-site diffusivity in BZ has also been addressed in connection with the chemical stability in CO_2-rich environments at elevated temperature.[10] Moreover, knowledge of cation transport is also vital for evaluating the long term stability of the materials in chemical potential gradients, which may induce kinetic demixing or decomposition.[11]

Cation diffusion in oxides is also interesting from a fundamental point of view. $BaZrO_3$ belongs to the family of $A^{II}B^{IV}O_3$ perovskites and among these perovskites, cation diffusion has so far only been experimentally investigated in $BaTiO_3$ (BT).[12] Several studies have investigated impurity diffusion in polycrystalline and single crystal BT with diverse results for the B-site.[13-16] The cations on A- and B-sites were reported to be almost equally mobile.[16] Ba diffusion in BT has also been reported,[17, 18] while experimental data on Ti diffusion is lacking. According to computational study on Ba and Ti migration in bulk BT, the activation energy for Ti diffusion is significantly higher than for Ba.[19]

With these aspects in mind, we present the first systematic report on cation tracer diffusion of ^{96}Zr and ^{134}Ba tracers in polycrystalline $BaZrO_3$ measured by Secondary Ion Mass Spectrometry (SIMS). The experimental data were obtained by annealing dense pellets of BZ coated with films of $^{96}ZrO_2$ or ^{134}BaO. The SIMS depth profiles were analysed to determine lattice and grain boundary diffusion coefficients and their corresponding activation energies. Furthermore, the activation energies of Ba^{2+} and Zr^{4+} diffusion were evaluated considering various diffusion paths and mechanisms by density functional theory (DFT) calculations using the nudged elastic band (NEB) method. The cation diffusion data were discussed with respect to the mobility of cations in the A- and B-sites of the perovskite lattice and the long term stability of electrochemical devices based on BZ electrolytes. Finally, diffusion of Zr in $BaZrO_3$ was compared to the corresponding diffusion in ZrO_2-based fluorite materials.

2 Experimental

2.1 Sample preparation

Dense $BaZrO_3$ ceramics were prepared from fine and homogeneous powder synthesized by spray pyrolysis

[a] Department of Materials Science and Engineering, NTNU Norwegian University of Science and Technology, NO-7491, Trondheim, Norway.
[b] Research Center for Functional Materials, National Institute for Materials Science, 1-1 Namiki, Tsukuba 305-0044, Japan.
[c] Centre for Materials Science and Nanotechnology (SMN), FERMiO, Department of Chemistry, University of Oslo, NO-0349 Oslo, Norway.
[d] SINTEF Materials and Chemistry, PO Box 124 Blindern, NO-0314 Oslo, Norway.
Electronic Supplementary Information (ESI) available: See DOI: 10.1039/x0xx00000x

(CerPoTech AS, Norway). The pre-consolidation, consolidation and sintering procedure of the ceramics have been described recently.[10] The pellets were sintered at 1600 °C for 10 h covered in sacrificial powder consisting of BZ and 10 wt% $BaCO_3$ to avoid the loss of BaO. The surface of the sintered pellets was thoroughly polished with a diamond suspension (down to ¼ µm grade) to obtain a flat and smooth surface. Prior to deposition of the tracers, the BZ pellets were pre-annealed at 900 °C for 8 h in synthetic air to clean the surfaces and to remove any possible traces of carbonates and water.

Films containing the stable isotopes of ^{134}Ba or ^{96}Zr were deposited according to the procedure described in the supporting information. Isotope tracers in the form of $^{134}BaCO_3$ and $^{96}ZrO_2$ (Trace Sciences International, Canada) were transferred to nitrate-based solutions, which were deposited and thermally decomposed on the surface of the BZ pellets giving dense layers of the tracer oxides. These coated BZ pellets were subjected to diffusion anneals at 1015-1200 and 1300-1500 °C for ^{134}Ba and ^{96}Zr diffusion, respectively. The annealing time ranged between 1-90 h based on corresponding diffusion data for $BaTiO_3$.[15]

The sintered BZ pellets with tracer oxide layers were characterized by X-ray powder diffraction (XRD) using a DaVinci2 diffractometer with $CuK_{\alpha1}$ radiation. The microstructure of the materials before and after coating y the tracers was characterized using a Hitachi S3400N scanning electron microscope (SEM). The chemical composition of the tracer layers was confirmed by Energy Dispersive X-ray Spectroscopy (EDS). The grain size of the sintered ceramics was determined from the SEM images using the linear intercept method.

2.2 Secondary ion mass spectrometry

The distribution of the isotopes ^{134}Ba, ^{138}Ba, ^{96}Zr and ^{90}Zr in the BZ pellets was measured by secondary ion mass spectrometry (SIMS) using a Cameca IMS 4f instrument. A primary ion beam of 10 keV Cs^+ was applied in most of the measurements, while some experiments were performed with 12.5 keV O_2^+ ion beam. Cs^+ ion beam was chosen due to faster sputtering, deeper craters, larger raster size, less charging effect and more stable profiles. The primary ion current varied between 30 and 60 nA. Depending on the secondary ion intensities, an area with a diameter of ~30 µm in the center of a sputtered area of 100 × 100 µm^2 was gated for the signal detection and analysis in order to avoid negative interferences (edge and wall effects). An electron shower with acceleration of 4.5 kV for ~1.2 mA sample current was used due to the poor electrical conductivity of BZ. Dynamic transfer optics setting (DTOS) was used in 60 %. The secondary molecular $^{134}BaO^-$, $^{138}BaO^-$, $^{90}ZrO^-$, and $^{96}ZrO^-$ ion signals were measured as a function of the cycles per second (cps) and sputter time. In general, all the isotopes were recorded, each with a continuing average time of 2 s. Signal noise in the raw depth profiles was observed only for low intensity levels which indicates stable conditions for the SIMS analysis. The final depth profiles of the isotope tracer were normalized by subtraction of the isotopic ratio of natural abundance[20] to avoid instrumental variations, as described in equations (1)–(3),

$$[^{z}\mathrm{M}_{\mathrm{norm}}] = \frac{\mathrm{I}(^{z}\mathrm{MO}^-)}{\mathrm{I}(^{z+n}\mathrm{MO}^-)} - [^{z}\mathrm{M}_{\mathrm{NatAb}}] \quad (1)$$

$$[^{134}\mathrm{Ba}_{\mathrm{NatAb}}] = \frac{[^{134}\mathrm{Ba}]_{\mathrm{NatAb}}}{[^{138}\mathrm{Ba}]_{\mathrm{NatAb}}} = \frac{0.0242}{0.7170} \approx 0.034 \quad (2)$$

$$[^{96}\mathrm{Zr}_{\mathrm{NatAb}}] = \frac{[^{96}\mathrm{Zr}]_{\mathrm{NatAb}}}{[^{90}\mathrm{Zr}]_{\mathrm{NatAb}}} = \frac{0.0281}{0.5145} \approx 0.054 \quad (3)$$

where [^{z}M$_{norm}$] is normalized concentration of the tracer; I(^{z}MO$^-$) is SIMS intensity of the tracer molecular ion; I($^{z+n}$MO$^-$) is SIMS intensity of the most abundant isotope molecular ion and [^{z}M$_{NatAb}$] is isotopic ratio of natural abundance of the element. The crater depth was measured with a 3D Laser Scanning Confocal Microscope KEYENCE VK-X100. The maximum crater depth was 15 µm and no considerable roughness at the bottom of the crater was observed.

The lattice and grain boundary diffusion coefficients were determined by using two separate regions of the SIMS profiles. The lattice diffusion coefficients were obtained by fitting the first part of the tracer depth profile to a solution of Fick's second law in the case of a thin film source (Equation 4)[11, 21]

$$-\frac{\partial \ln[^{z}\mathrm{M}_{\mathrm{norm}}]}{\partial x^2} = -\frac{1}{4D_L t} \quad (4)$$

where, D_L is the lattice diffusion coefficient (cm^2 s^{-1}) of isotope ^{z}M with normalized concentration [^{z}M$_{norm}$] in depth x (cm) at time t (s). The grain boundary diffusion coefficients were determined from the shallow region of the depth profiles, at a longer diffusion length, using the Whiple-Le Clair's equation[11, 22]

$$s\delta D_{GB} = 1.322\sqrt{\frac{D_{eff}}{t}}\left(-\frac{\partial \ln[^{z}\mathrm{M}_{\mathrm{norm}}]}{\partial x^{6/5}}\right)^{-5/3} \quad (5)$$

where, s is a segregation factor, δ is the grain boundary width (cm), D_{GB} is the grain boundary diffusion coefficient (cm^2 s^{-1}), D_{eff} is an effective diffusion coefficient (cm^2 s^{-1}) and t is the annealing time (s). The diffusion coefficients along grain boundaries were calculated using δ=1 nm and s=1, values typically used in similar tracer diffusion studies. The effective diffusion coefficient, D_{eff}, represents a combined lattice and grain boundary diffusivity, calculated by $D_{eff} = gD_{GB} + D_L$ where $g = 3\delta/d$.

3 Computational details

The DFT calculations were performed using the projector-augmented wave (PAW) method with the Perdew-Burke-Ernzerhof generalized gradient approximation (GGA-PBE) functional as well as the nudged elastic band (NEB) method to determine the activation energy of diffusion as implemented into Vienna *Ab initio* Simulation Package (VASP).[23-26] The calculations were performed with a 500 eV plane-wave energy cut-off and the ionic positions were optimized until the residual

forces were within 0.02 eV $Å^{-1}$ for the unit cell and 0.05 eV $Å^{-1}$ for the NEB calculations. The self-consistent electronic optimization was performed with an energy convergence criterion of 10^{-6} eV. The supercell used was a 4×4×4 expansion of the optimized unit cell with a total of 320 atoms and with k-points sampled according to a 2×2×2 Monkhorst-Pack grid.[27] The site fraction of the cation vacancies in the supercell was 1/64. The cation vacancies were fully ionized and charge compensated by a uniform background charge that was constant throughout the migration path.[28]

4 Results

A representative micrograph of the BZ ceramics is shown in Figure 1. The sintered ceramics were phase pure BZ with a grain size of 1.1±0.1 µm and >97 % relative density. The diffraction pattern of the sintered BZ material is shown in Figure 2, and the cubic unit cell parameter 4.193±0.001 Å, obtained by Rietveld refinement, is in good accord with literature.[29]

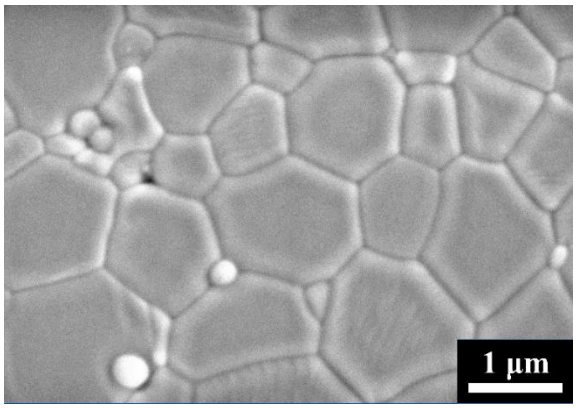

Figure 1. The microstructure of the sintered and thermally etched BZ ceramic. Gracing incident X-ray diffraction and EDS confirmed that the small grains in the image are also pure BZ.[10]

Considerable effort was spent to develop a procedure for deposition of phase pure, homogeneous and crack free films of $^{96}ZrO_2$ and ^{134}BaO, referred to as ZrO_2 and BaO in the following. The films with the highest quality were achieved by a single step drop casting of $ZrO(NO_3)_2$ or $Ba(NO_3)_2$ solutions followed by thermal annealing to obtain oxide films. The XRD patterns of the surface of the coated pellets showed layers of monoclinic ZrO_2 or cubic BaO (Figure 2). The 1-2 µm thick polycrystalline tracer films were close to phase pure except minor amounts of $BaCO_3$ and $BaSO_4$ in case of ZrO_2. The distribution of the two tracers was homogeneous and the films exhibited good physical attachment to the surface of the BZ pellets (see supporting information).

The SIMS raw data for the depth profiles of ^{134}Ba and ^{96}Zr in BZ after annealing at 1050 °C for 35 h and 1450 °C for 4 h, respectively, are given in Figure 3. The graphs show the logarithmic intensities of the secondary ions $^{134}BaO^-$, $^{138}BaO^-$, $^{90}ZrO^-$, and $^{96}ZrO^-$ as a function of the normalized depth. The depth profiles demonstrate clear differences between the tracer and the most abundant isotopes. The measured concentration of the tracers became essentially constant at levels close to the natural abundances of ^{96}Zr and ^{134}Ba. The diffusion profiles of the normalized logarithmic ^{96}Zr concentration are shown in Figure 4. There is no evident trend with respect to the annealing temperature due to the variation in the annealing time. The normalized profiles exhibit higher noise levels when the natural abundance of the tracer is approached at a penetration depth of a few microns into the bulk (Figure 4).

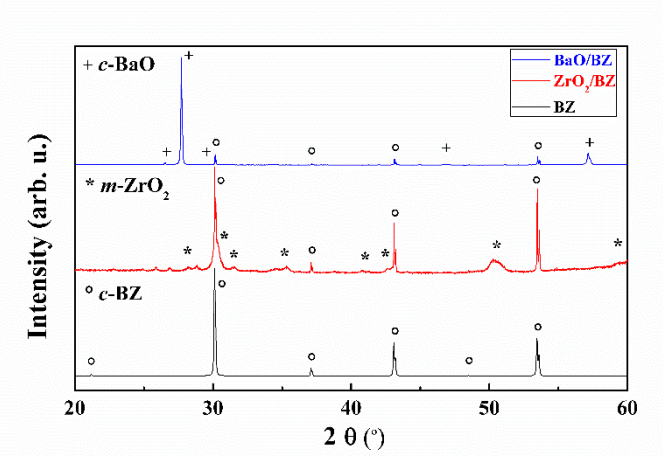

Figure 2. XRD patterns of the pristine BZ[29] and BZ coated with ZrO_2 (JPPDS card 36-0420) and BaO (89-8425). Traces of $BaCO_3$ (45-1471) and $BaSO_4$ (24-1035) are not shown for simplification.

^{96}Zr depth profiles of the regions related to bulk and grain boundary diffusion are given in Figure 5 for the diffusion anneal at 1450 °C for 4 h. The data is plotted as function of x^2 and $x^{6/5}$ in the two regions according to Equations (4) and (5) with fits to the data shown by the red curves. The fitting procedure of the ^{134}Ba depth profiles was similar and is described in the supporting information. The penetration depth of the tracers into the grains of the pellets was of the same magnitude or shorter than the average grain size. The resulting data for the bulk and grain boundary diffusion coefficients for both tracers are summarized in Table S1 in supporting information. The criteria for using Equation (5) to determinate the grain boundary diffusion coefficients for all the cases were also fulfilled (see supporting information).[22, 30]

The logarithm of the tracer diffusion coefficients of ^{134}Ba and ^{96}Zr in BZ annealed in air as a function of reciprocal temperature are summarized in Figure 6. The diffusion coefficients for both ^{134}Ba and ^{96}Zr follow an Arrhenius behaviour. The activation energy determined by the linear fit to the data (see also supporting information) is summarized in Table 1. The grain boundary diffusion coefficients are 4–5 orders of magnitude higher than corresponding data for lattice diffusion, and the activation energy is 80–90 kJ mol^{-1} lower than for the lattice diffusion. The activation energies for Zr diffusion are 40–50 kJ mol^{-1} higher than for Ba.

The migration path for Ba^{2+} diffusion through a nearest neighbour vacancy mechanism used in the DFT calculations is shown in Figure 7a. The Ba vacancy is the most likely dominating

cation point defect in BZ.[31] The activation energy was calculated to be 4.1 eV (Figure 7b), which is in excellent agreement with the experimental value (Table 1).

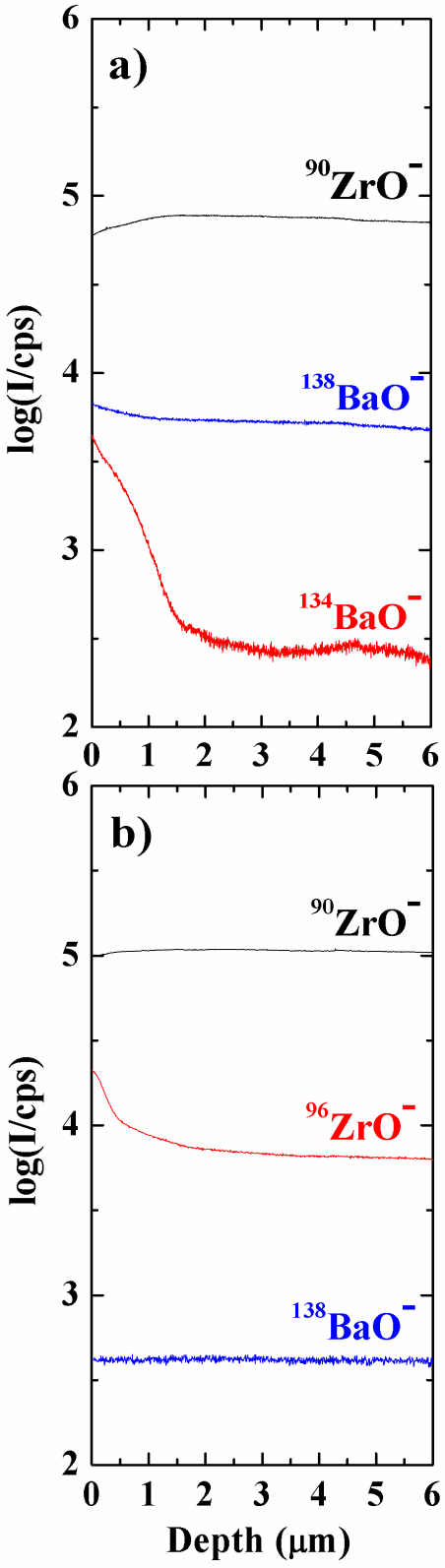

Figure 3. SIMS depth profiles for (a) ^{134}Ba and (b) ^{96}Zr diffusion in polycrystalline BZ.

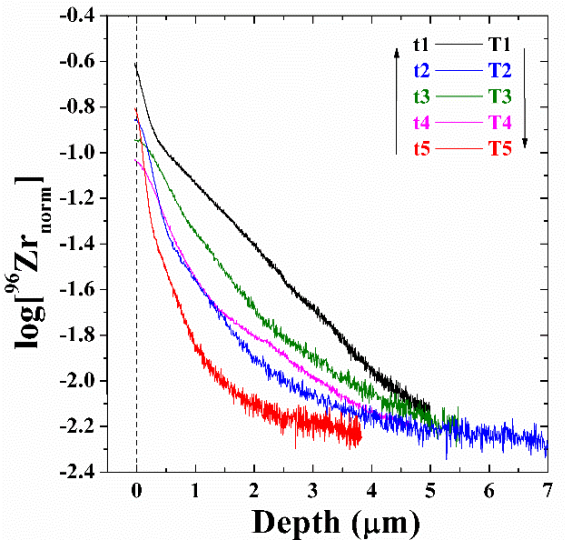

Figure 4. Normalized logarithmic concentration of the ^{96}Zr tracer in BZ as a function of the penetration depth, annealing temperature (T) and time (t). The annealing time increased with decreasing annealing temperature, see supporting information.

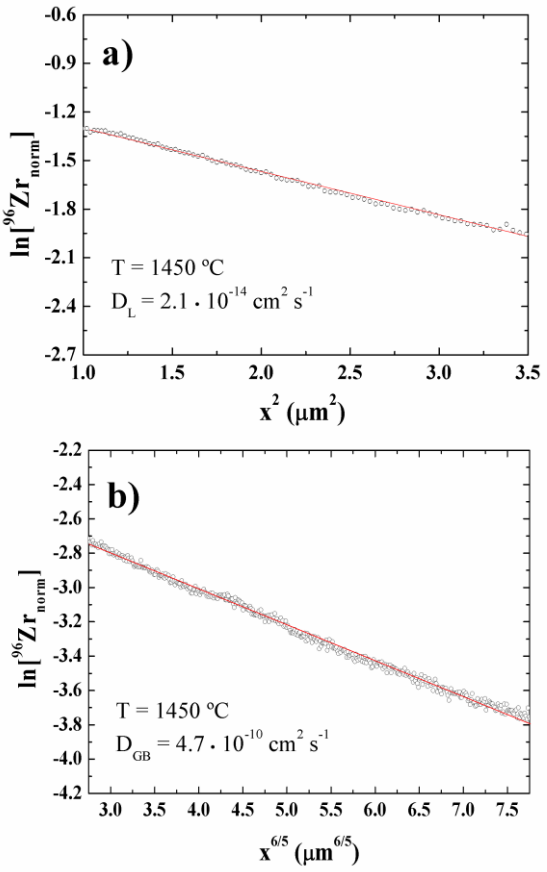

Figure 5. Examples of the fitting of the normalized tracer profile of ^{96}Zr in BZ for (a) lattice and (b) grain boundary diffusion.

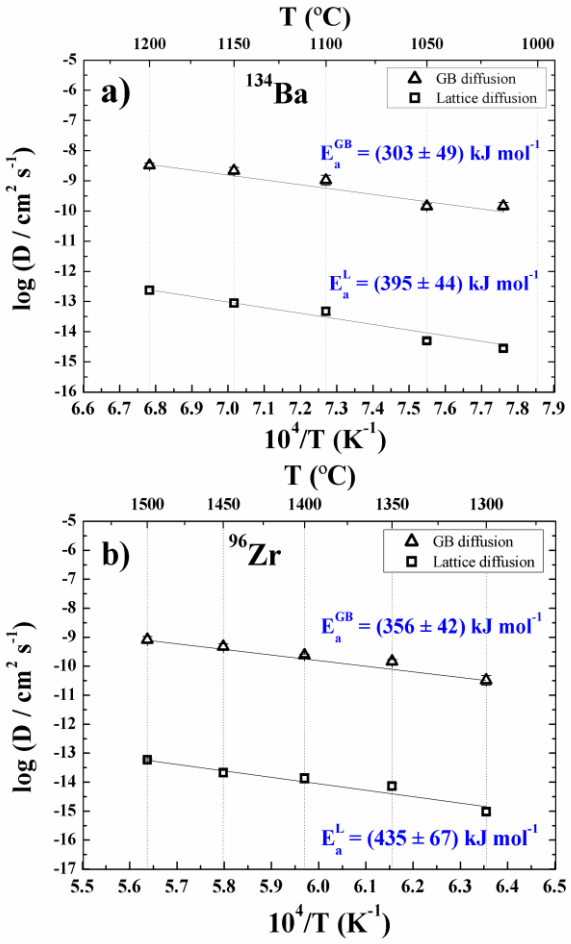

Figure 6. Arrhenius plots for (a) ^{134}Ba and (b) ^{96}Zr diffusion in BZ. The uncertainty for each data point is calculated as the standard deviation for D_o and E_a.

In the case of Zr^{4+} diffusion, the activation energy calculated for a nearest neighbour vacancy mechanism was found to be far larger than the experimental value (>10 eV) clearly indicating a different diffusion mechanism. By introducing a Ba vacancy on the diagonal between the initial and final Zr position, migration was facilitated and the calculated activation energy was 4.3 eV (Figure 8) in excellent agreement with the experimental value (Table 1).

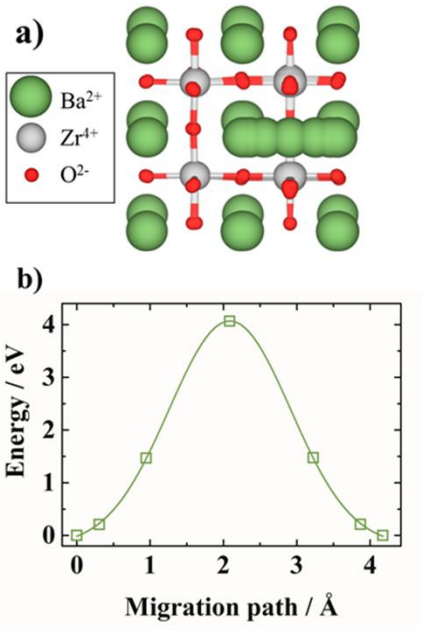

Figure 7. The migration path (a) and energy barrier (b) for the Ba^{2+} migration facilitated via a Ba vacancy. Each calculated energy shown in b corresponds to the positions of Ba^{2+} along the migration path shown in a, from left to right.

5 Discussion

Ionic diffusion in solids depends on point defects in the crystal lattice. The most prominent point defects in $BaZrO_3$ at the present experimental conditions are oxygen vacancies ($v_O^{\bullet\bullet}$), Ba vacancies (v_{Ba}''), Zr vacancies ($v_{Zr}^{4\prime}$)[31] and possibly Zr anti-site ($Zr_{Ba}^{\bullet\bullet}$) as discussed for $SrTiO_3$.[32] Cation interstitials are usually considered to be of limited importance in perovskites, although small transition metals may dissolve interstitially in Ba-deficient BZ.[33] Point defects in stoichiometric BZ are formed through the Schottky point defect equilibrium

$$\text{nill} \rightarrow v_{Ba}'' + v_{Zr}^{4\prime} + 3v_O^{\bullet\bullet} \qquad (6)$$

Table 1. The experimental activation energy and pre-exponential factor for ^{134}Ba and ^{96}Zr diffusion in polycrystalline BZ found by fitting the SIMS data to the Arrhenius equation. The errors given are the standard deviation obtained by the regression analysis including the error for each data point in Figure 6. The activation energies determined by DFT calculations are given for comparison.

Site	Tracer	Temperature (°C)	Diffusion location	D_o ($cm^2\ s^{-1}$)	$E_{a\ experimental}$ (kJ mol^{-1})	(eV)	$E_{a\ computational}$ (eV)
A	^{134}Ba	1015-1200	Lattice	30.0±1.3	395±44	4.1±0.5	4.1
			GB	230.0±1.6	303±49	3.1±0.5	
B	^{96}Zr	1300-1500	Lattice	0.4±1.2	435±67	4.5±0.7	4.3
			GB	28.0±1.3	356±40	3.7±0.4	

The formation of Ba and O vacancies have been argued from loss of BaO during sintering,[34] described by the point defect equilibrium

$$Ba_{Ba}^{x} + O_{O}^{x} \rightarrow v_{Ba}'' + v_{O}^{\bullet\bullet} + BaO(g) \quad (7)$$

Ba vacancies (v_{Ba}'') and oxygen vacancies ($v_{O}^{\bullet\bullet}$) are therefore most likely the dominant point defects in BZ-based materials due to cation non-stoichiometry. A minor concentration of Zr vacancies is also present due to the equilibration of the Schottky equilibrium (6) during sintering at 1600 °C.

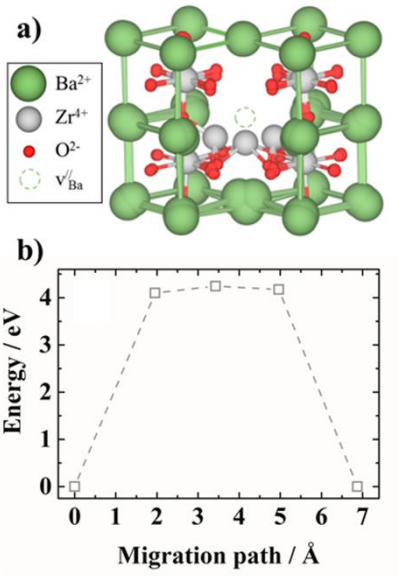

Figure 8. The migration path (a) and energy barrier (b) for the Zr^{4+} migration facilitated by the presence of a Ba vacancy. Each calculated energy shown in b corresponds to the positions of Zr^{4+} along the migration path shown in a, from left to right.

The possible diffusion pathways for Ba and Zr cations, and the point defects involved in each case, are illustrated in Figure 9. The two first (A, B) illustrate possible paths for Ba though a Ba-vacancy or a Zr vacancy, where the latter is less likely due to the size mismatch of the two cations.[32] Possible pathways for Zr are through a Ba vacancy, a combination of a Ba and Zr vacancy and finally through a Zr-vacancy. The excellent agreement between the calculated and experimentally determined activation energies for bulk diffusion of Ba supports that a diffusion pathway for Ba through Ba-vacancies (Figure 9A) is the most likely diffusion mechanism for Ba and other A-site cations in BZ. Both the formation of point defects and migration may contribute to the experimental determined activation energy. However, the excellent agreement between the calculated activation energy of migration and the experimental values points to a low contribution from the formation of point defects in the temperature range of the experiments. This can be understood from the long relaxation time of the Schottky defect equilibrium (6), relative to the annealing time at these conditions due to the slow diffusion of the cations as demonstrated in this study.

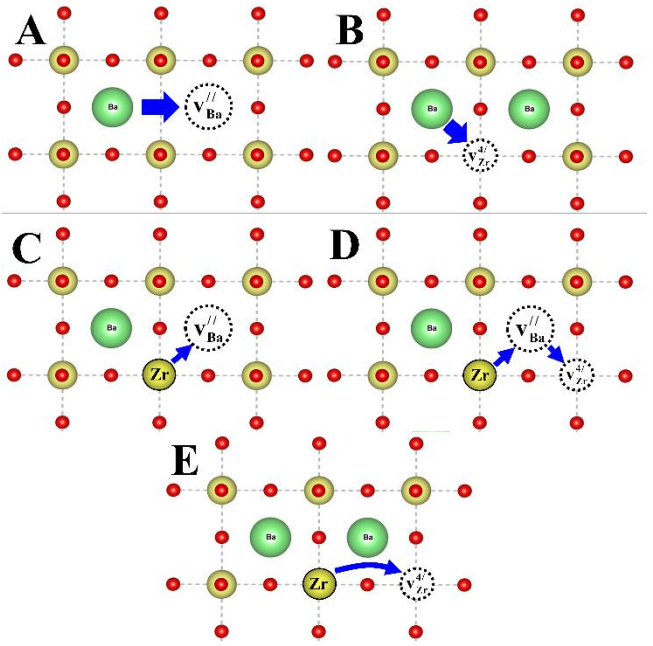

Figure 9. A schematic of diffusion pathways in nonstoichiometric BZ for barium (A-B) and zirconium (C-E): A) Ba diffusion via Ba vacancy; B) Ba diffusion via Zr vacancy; C) Zr diffusion via Ba vacancy; D) Zr diffusion via Ba and Zr vacancies; E) Zr diffusion via Zr vacancy.

The calculated activation energy for Zr-diffusion points to Zr-diffusion facilitated by a vacant Ba-site (Figure 9D). The activation energy is in very good agreement with the experimental data (Table 1), and activation energy calculated for other pathways was calculated far higher than the experimental value. This diffusion mechanism for Zr in BZ is similar to the mechanism reported for Ti diffusion in $SrTiO_3$.[35] Also in case of Zr diffusion one can argue that there is little contribution from the formation of point defects to the activation energy.

The nudge elastic band DFT calculations reported here for both migration of Ba and Zr takes into account the contribution from local variation in the symmetry and charge distribution to the activation barrier for the diffusion of both type of cations. The conclusion from the DFT calculations is that both cations diffuse through a vacant Ba-site.

Lattice diffusion of Ba is faster than Zr in BZ, showing that the ionic size and charge are important factors for the ionic mobility in the lattice, which is related to the oxidation state of the cations and the coordination number of the cations in the two sites in the perovskite lattice. The activation energies for diffusion of the two cations were found to be quite similar (Table 1).

This study also shows that the grain boundary diffusion is significantly faster than the lattice diffusion for both cations, which has been reported for a whole range of perovskite materials and other oxides.[36, 37] The explanation for the faster diffusion along grain boundaries can be related both to lower energy of formation of point defects at the grain boundaries and lower activation energy for migration. If we assume that the

energy of formation of point defects contribute less to the experimental data as suggested for lattice diffusion, it can be argued that the activation energy for migration of cations along grain boundaries are lower than through the lattice.

The Ba lattice diffusion in $BaZrO_3$ is compared to the A-site cation mobility in selected perovskites in Figure 10.[15, 30-40] Literature data on A-site diffusion in perovskites is scarce and there is no apparent trend in the A-site diffusivity. From a structural point of view the size and charge of the cations and thereby the tolerance factor and structural distortions of the perovskite lattice will influence the activation energy for diffusion. However, the point defect chemistry, which is influenced by material processing, determine the dominating diffusion mechanism as shown for BZ. The diffusion mechanisms for the data reported in the literature are in most cases not determined. It can be seen in Figure 10 that diffusion of the A-site cation is faster in BZ than in polycrystalline $BaTiO_3$ but slower than in $SrTiO_3$. The A-site diffusion is also faster in polycrystalline BZ compared to A-site diffusion in chromate-perovskites, while slower than in cobaltates or ferrates, which all are $A^{III}B^{III}O_3$ perovskites with a low tolerance factor relative to BZ. The A-site diffusion in $A^{II}B^{IV}O_3$ perovskites including BZ possesses higher activation energies than for $A^{III}B^{III}O_3$ perovskites. Finally, the mobility of Ba in rock-salt BaO is included in Figure 10, showing that Ba diffusion in this material is faster than in Ba-based perovskites.

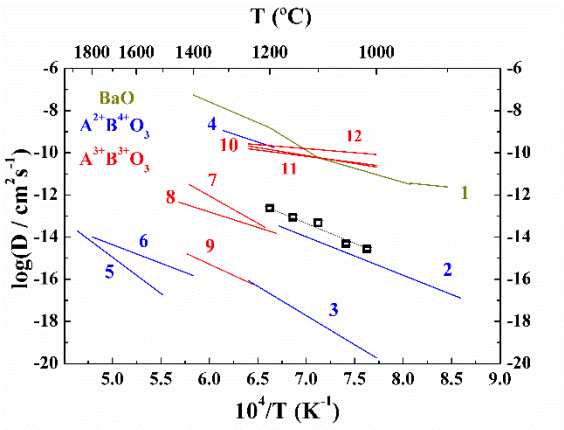

Figure 10. Arrhenius type plot of A-site diffusion coefficients in BZ compared to literature data for selected perovskites and BaO.[15, 38-48] Abbreviations: p – polycrystalline; sc – single crystal; c – cubic. 1) ^{133}Ba in BaO [38]; 2) ^{131}Ba in p $BaTiO_3$ [39]; 3) Sr in sc $BaTiO_3$ [15]; 4) ^{90}Sr in p $SrTiO_3$ [40]; 5) ^{88}Sr in sc $SrTiO_3$ [41]; 6) Mg in $MgSiO_3$ [44]; 7) La in $LaCrO_3$ [42]; 8) Y in $YCrO_3$ [43]; 9) Pr in $PrCoO_3$ [45]; 10) Sm in $SmCoO_3$ [45]; 11) Eu in $EuCoO_3$ [45]; 12) Nd in $NdCoO_3$ [46].

The Zr diffusion coefficient in $BaZrO_3$ is compared to corresponding data for B-site diffusion in perovskites in Figure 11.[38, 48-49] The B-site diffusivity is lower in BZ than in in tetragonal $BaTiO_3$ with a tolerance factor larger than 1. In contrast, the B-site diffusion in BZ is slower than in most of the $A^{III}B^{III}O_3$ perovskites. The reason could be attributed to the higher charge of the B-site cation and a larger tolerance factor for BZ. The lack of knowledge about the diffusion mechanisms in most of the data reported for the $A^{III}B^{III}O_3$ compounds is also making the direct comparison of diffusion data challenging. It can also be noted that the activation energy for BZ is higher than that for $A^{III}B^{III}O_3$ perovskites. The high charge of the B-cations in $A^{II}B^{IV}O_3$ perovskites such as BZ reduce the diffusivity of B-cations.

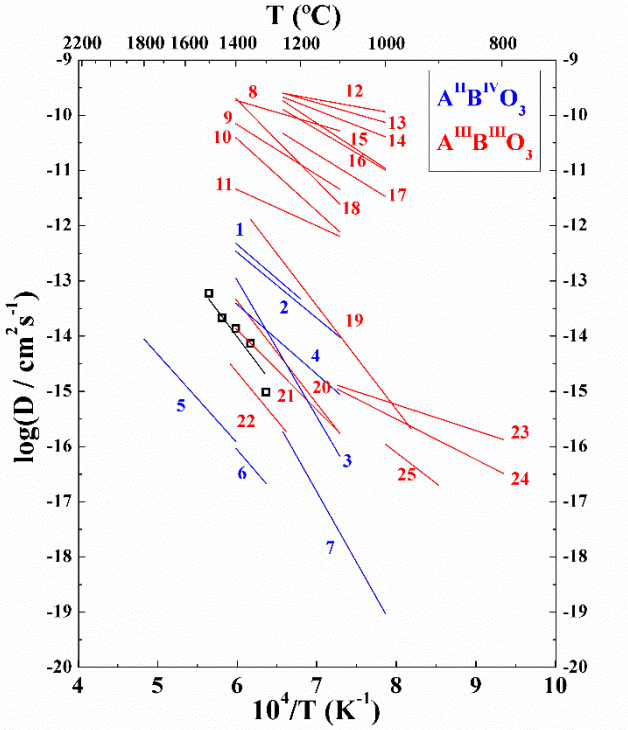

Figure 11. Arrhenius type plot of B-site diffusion coefficients in BZ compared to the literature for $A^{II}B^{IV}O_3$ and $A^{III}B^{III}O_3$ perovskites. Abbreviations: p – polycrystalline; sc – single crystal; c – cubic. [13-15, 45, 37-50] 1) Ho in p $BaTiO_3$ b [14]; 2) Ni in p $Ba(Ho,Ti)O_3$ [13]; 3) Ni in sc $BaTiO_3$ [13]; 4) Ni in p $BaTiO_3$ [13]; 5) Si in $MgSiO_3$ [44]; 6) ^{49}Ti in sc $(La,Sr)TiO_3$ [51]; 7) Zr in sc $BaTiO_3$ [15]; 8) Cr in $LaMnO_3$ [52]; 9) Mn in $LaCoO_3$ [53]; 10) Co in $LaCoO_3$ [45]; 11) ^{141}Pr in $LaMnO_3$ [37]; 12) Co in $GdCoO_3$ [45]; 13) Co in $EuCoO_3$ [45]; 14) Co in $SmCoO_3$ [45]; 15) Co in $NdCoO_3$ [45]; 16) Co in $PrCoO_3$ [45]; 17) Co in $LaCoO_3$ [54]; 18) Mn in $LaMnO_3$ [52]; 19) Fe in $LaFeO_3$ [55]; 20) ^{141}Pr in $LaCoO_3$ [37]; 21) ^{141}Pr in $LaFeO_3$ [37]; 22) Fe in $NdFeO_3$ p [46]; 23) Fe in $(La,Sr)CoO_3$ [56]; 24) Fe in $(La,Sr)FeO_3$ [56]; 25) ^{50}Cr in $(La,Ca)CrO_3$ [50].

The diffusion coefficients of the materials with fluorite structure are summarized in Figure 12 and compared to the experimental results for Zr^{4+} diffusion coefficients from this study. The diffusion coefficient of zirconium in the $BaZrO_3$ perovskite is of the same order of magnitude as Zr diffusion in fluorite-type oxides.

In comparison to the other materials, the B-site lattice diffusion coefficients in $BaZrO_3$ are lower than in $LaBO_3$-materials (B = Co, Fe, Mn), which have been investigated with respect to kinetic demixing phenomena.[52, 57] Kinetic demixing is critical for the lifetime of gas separation membranes and electrolytes when operated for a long time at elevated

Figure 12. Arrhenius type plot of Zr lattice and grain boundary

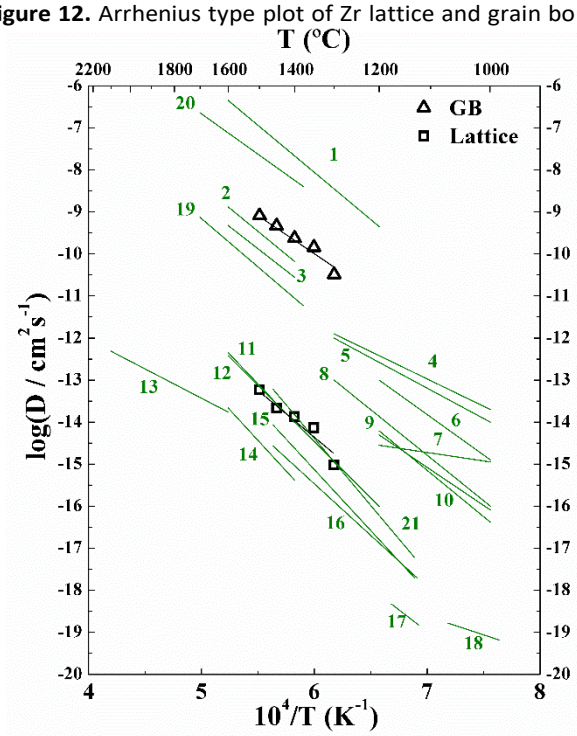

diffusion coefficients in BZ compared to literature for fluorites. [38, 48-49, 59-60] Abbreviations: p – polycrystalline; sc – single crystal; c – cubic; b – bulk; gb – grain boundaries.
1) ^{96}Zr in c-ScSZ gb [59]; 2) Yb in t-YSZ gb [36]; 3) Hf in T-YSZ gb [36]; 4) Fe in $(Gd,Ce)O_2$ [61]; 5) Co in $(Gd,Ce)O_2$ [61]; 6) La in $(La,Ce)O_2$ [61]; 7) Co in $(La,Ce)O_2$ [61]; 8) Sr in $(Gd,Ce)O_2$ [62]; 9) Sr in $(Gd,Ce)O_2$ [60]; 10) La in $(Gd,Ce)O_2$ [60]; 11) Yb in t-YSZ b [36]; 12) ^{96}Zr in c-ScSZ b [59]; 13) ^{230}Th in ThO_2 [38]; 14) Hf in T-YSZ b [36]; 15) ^{96}Zr in c-CSZ sc [48]; 16) ^{96}Zr in c-YSZ sc [48]; 17) Gd in CeO_2 gb [49]; 18) Gd in CeO_2 b [49]; 19) ^{88}Y in c-YSZ b [48]; 20) ^{88}Y in c-YSZ gb [48]; 21) ^{44}Ca in c-CSZ [48].

temperature, and is particularly dependent on time and thickness of the material.[58] Reduced thickness results in a higher gradient in the chemical potential and a larger driving force for diffusion. Kinetic demixing is controlled by the fastest diffusing species and the differences in mobility among the cations. Thus, barium and particularly grain boundary diffusion of Ba is important for kinetic demixing in BZ. Kinetic demixing and decomposition in $LaBO_3$-materials has been reported at 1100 °C.[58] Taking into account the rather low lattice and GB diffusion coefficients in BZ, relative to $LaBO_3$-materials (see Figure 11), the possibility for kinetic demixing in BZ is low when considering operation temperatures around 500–600 °C. Consequently, $BaZrO_3$-materials are foreseen to be robust in terms of cation diffusion especially emphasising the slow Zr diffusion.[10]

The slow diffusion of the B-site cations is also most likely the rate limiting process in sintering and the main reason for the necessity of high sintering temperatures to achieve high density BZ. The sintering of BZ become more challenging with Y-doping[8,9], which point to even lower diffusivity of Zr in BZ when acceptor doped. The use of sintering additives to reduce the sintering temperature of BZ is most likely related to grain boundary diffusion and not due to increased bulk diffusion of cations. The higher mobility of Ba relative to Zr should be addressed with respect to heterogeneous phase equilibria at the surface as recently demonstrated by formation of $BaCO_3$ in BZ-materials in CO_2 atmosphere.[10]

Conclusions

The lattice and grain boundary diffusion of both A- and B-site cations in polycrystalline BZ were determined by tracer diffusion experiments. The lattice diffusion coefficients of Ba were higher than those of Zr in the temperature region investigated (1015–1500 °C), with activation energies of 395±44 kJ·mol^{-1} and 435±67 kJ·mol^{-1}, respectively. It was concluded based on DFT calculations that bulk diffusion of both cations is facilitated by the presence of Ba-vacancies. Enhanced diffusivity along grain boundaries was observed for both Ba and Zr with activation energies of 303±49 kJ·mol^{-1} and 356±40 kJ·mol^{-1}, respectively. The bulk diffusivities reported for BZ are lower than for other $A^{II}B^{IV}O_3$ and most of the $A^{III}B^{III}O_3$ perovskites reported in the literature. The Zr-diffusivity in BZ is comparable to the Zr-diffusivity in most fluorites, such as YSZ, which suggests that BZ is a robust material with respect to B-site diffusivity. The low diffusivity of cations in BZ, particularly Zr, support that BZ-based electrolytes is stable in electrochemical potentials at elevated temperatures.

Acknowledgements

Financial support from NIMS - International Cooperative Graduate Program and The Research Council of Norway under the program NANO2021 to the project (Number 228355) "Functional oxides for clean energy technologies: fuel cells, gas separation membranes and electrolyzers" (FOXCET) conducted by SINTEF Materials and Chemistry, University of Oslo and The Norwegian University of Science and Technology (NTNU) in Trondheim, is gratefully acknowledged. Computational resources were provided by the Norwegian Metacentre for Computational Science (NOTUR) under the project nn4604k.

Author contributions: RS performed all the experiments. TG supervised the experimental work. IS supervised the SIMS experiments. IH performed the DFT calculations supervised by JP. RS wrote the paper with discussion and contributions from all the authors.

References

1 E. C. C. d. Souza and R. Muccillo, *Mater. Res.*, 2010, **13**, 385.
2 J. W. Phair and S. P. S. Badwal, *Sci.Tech. Adv. Mater.*, 2016, **7**, 792.
3 L. Malavasi, C. A. Fisher and M. S. Islam, *Chem. Soc. Rev.*, 2010, **39**, 4370.
4 N. Kochetova, I. Animitsa, D. Medvedev, A. Demin and P. Tsiakaras, *RSC Adv.*, 2016, **6**, 73222.

5 K. D. Kreuer, *Ann. Rev. Mater. Res.*, 2003, **33**, 333.
6 K. D. Kreuer, *Solid State Ionics*, 1997, **97**, 1.
7 Y. Oyama, A. Kojima, X. Li, R. B. Cervera, K. Tanaka and S. Yamaguchi, *Solid State Ionics*, 2011, **197**, 1.
8 D. Han, K. Kishida, K. Shinoda, H. Inui and T. Uda, *J. Mat. Chem. A*, 2013, **1**, 3027.
9 Y. Yamazaki, C.-K. Yang and S. M. Haile, *Scripta Materialia*, 2011, **65**, 102.
10 R. Sazinas, C. Bernuy-Lopez, M. A. Einarsrud and T. Grande, *J. Am. Ceram. Soc.*, 2016, **99**, 3685.
11 V. V. Kharton, *Solid state electrochemistry II*, Ist, Willey-VCH, Weinheim, Germany, 2011.
12 J. Bera and S. K. Rout, *Mater. Lett.*, 2005, **59**, 135.
13 J.-i. Itoh, I. Yashima, N. Ohashi, I. Sakaguchi, H. Haneda and J. Tanaka, *J. Ceram. Soc. Jpn.*, 2001, **109**, 955.
14 J. Itoh, H. Haneda, S. Hishita, I. Sakaguchi, N. Ohashi, D.-C. Park and I. Yashima, *J. Mater. Res.*, 2004, **19**, 3512.
15 S. Koerfer, R. A. De Souza, H.-I. Yoo and M. Martin, *Solid State Sciences*, 2008, **10**, 725.
16 H.-I. Yoo, C.-E. Lee, R. A. De Souza and M. Martin, *App. Phys. Lett.*, 2008, **92**, 252103.
17 W. M. Robertson, *J. Nuclear Mater.*, 1969, **30**, 36.
18 A. Kitahara, M. Nanko, K. Kawamura and T. Maruyama, *Per Kofstad Memorial Symposium on High Temperature Corrosion and Materials Chemistry at the 1999 Joint Int Meeting of the Electrochem-Soc/Electrochem-Soc-of-Japan,* Diffusion Coefficient of Ba^{2+} Ion in $BaTiO_3$, ELECTROCHEMICAL SOCIETY INC, 65 S MAIN ST, PENNINGTON, NJ 08534-2839 USA, HONOLULU, HI, 2000.
19 G. V. Lewis and C. R. A. Catlow, *Radiation Effects*, 1983, **73**, 307.
20 R. D. Vocke, *Pure and App. Chem.*, 1999, **71**, 1593.
21 J. Crank, *The Mathematics of Diffusion*, Oxford University Press, Oxford, 1975.
22 D. Gryaznov, J. Fleig and J. Maier, *J. App. Phys.*, 2008, **103**, 063717.
23 P. E. Blöchl, *Physical review B*, 1994, **50**, 17953.
24 G. Kresse and D. Joubert, *Physical Review B*, 1999, **59**, 1758.
25 J. P. Perdew, K. Burke and M. Ernzerhof, *Physical review letters*, 1996, **77**, 3865.
26 G. Henkelman, B. P. Uberuaga and H. Jónsson, *The Journal of chemical physics*, 2000, **113**, 9901.
27 H. J. Monkhorst and J. D. Pack, *Physical review B*, 1976, **13**, 5188.
28 M. A. Gomez, M. A. Griffin, S. Jindal, K. D. Rule and V. R. Cooper, *J. Chem. Phys.*, 2005, **123**, 94703.
29 S. Yamanaka, M. Fujikane, T. Hamaguchi, H. Muta, T. Oyama, T. Matsuda, S.-i. Kobayashi and K. Kurosaki, *J. All. Comp.*, 2003, **359**, 109.
30 I. V. Belova and G. E. Murch, *Defect and Diffusion Forum*, 2008, **273-276**, 425.
31 S. J. Stokes and M. S. Islam, *J. Mater. Chem.*, 2010, **20**, 6258.
32 K. Klyukin and V. Alexandrov, *Phys. Rev. B*, 2017, **95**, .
33 J. M. Polfus, M.-L. Fontaine, A. Thøgersen, M. Riktor, T. Norby and R. Bredesen, *J. Mater. Chem. A*, 2016, **4**, 8105.
34 P. Babilo, T. Uda and S. M. Haile, *J. Mater. Res.*, 2007, **22**, 1322.
35 T. Mizoguchi, N. Takahashi and H.-S. Lee, *App. Phys. Lett.*, 2011, **98**, 091909.
36 S. Swaroop, M. Kilo, C. Argirusis, G. Borchardt and A. H. Chokshi, *Acta Materialia*, 2005, **53**, 4975.
37 M. Palcut, J. S. Christensen, K. Wiik and T. Grande, *Phys. Chem. Chem. Phys.*, 2008, **10**, 6544.
38 R. Freer, *J. Mater. Sci.*, 1980, **15**, 803.
39 A. Garcia-Verduch and R. Lindner, *Arkiv. Kemi.*, 1953, **5**, 313.
40 W. H. Rhodes and W. D. Kingery, *J. Am. Ceram. Soc.*, 1966, **49**, 521.
41 K. Gömann, G. Borchardt, M. Schulz, A. Gömann, W. Maus-Friedrichs, B. Lesage, O. Kaïtasov, S. Hoffmann-Eifert and T. Schneller, *Phys. Chem. Chem. Phys.*, 2005, **7**, 2053.
42 T. Akashi, M. Nanko, T. Maruyama, Y. Shiraishi and J. Tanabe, *J. Electrochem. Soc.*, 1998, **145**, 2090.
43 K. i. Kawamura, A. Saiki, T. Maruyama and K. Nagata, *J. Electrochem. Soc.*, 1995, **142**, 3073.
44 J. Xu, D. Yamazaki, T. Katsura, X. Wu, P. Remmert, H. Yurimoto and S. Chakraborty, *J. Geophys. Res.*, 2011, **116**, .
45 A. N. Petrov, L. Y. Rabinovich, V. M. Zhukovskii and A. S. Zhukovskaia, *Dokl. Chem.* , 1987, **292** 18.
46 M. M. Pavlyuchenko, B. O. Filonov, I. E. Shimanovich and S. A. Produkina, *Dokl. Akad. Nauk BSSR*, 1970, **14**, 328.
47 M. Kilo, G. Borchardt, S. Weber, S. Scherrer, K. Tinschert, B. Lesage and O. Kaïtasov, *Radiation Effects and Defects in Solids*, 1999, **151**, 29.
48 M. Kilo, M. A. Taylor, C. Argirusis, G. Borchardt, B. Lesage, S. Weber, S. Scherrer, H. Scherrer, M. Schroeder and M. Martin, *J. App. Phys.*, 2003, **94**, 7547.
49 C. Rockenhäuser, B. Butz, N. Schichtel, J. Janek, R. Oberacker, M. J. Hoffmann and D. Gerthsen, *J. Eur. Ceram. Soc.*, 2014, **34**, 1235.
50 N. Sakai, K. Yamaji, T. Horita, H. Negishi and H. Yokokawa, *Solid State Ionics*, 2000, **135**, 469.
51 K. Gömann, G. Borchardt, A. Gunhold, W. Maus-Friedrichs and H. Baumann, *Phys. Chem. Chem. Phys.*, 2004, **6**, 3639.
52 S. Miyoshi and M. Martin, *Phys. Chem. Chem. Phys.*, 2009, **11**, 3063.
53 M. Palcut, R. Knibbe, K. Wiik and T. Grande, *Solid State Ionics*, 2011, **202**, 6.
54 M. Palcut, K. Wiik and T. Grande, *J. Phys. Chem. B*, 2007, **111**, 2299.
55 J. Smith and T. Norby, *Solid State Ionics*, 2006, **177**, 639.
56 H. Kishimoto, N. Sakai, T. Horita, K. Yamaji, M. Brito and H. Yokokawa, *Solid State Ionics*, 2007, **178**, 1317.
57 R. A. De Souza, M. Saiful Islam and E. Ivers-Tiffee, *J. Mater. Chem.*, 1999, **9**, 1621.
58 H. Lein, K. Wiik and T. Grande, *Solid State Ionics*, 2006, **177**, 1587.
59 M. A. Taylor, M. Kilo, G. Borchardt, S. Weber and H. Scherrer, *J. Eur. Ceram. Soc.*, 2005, **25**, 1591.
60 M. Izuki, M. E. Brito, K. Yamaji, H. Kishimoto, D.-H. Cho, T. Shimonosono, T. Horita and H. Yokokawa, *J. Pow. Sour.*, 2011, **196**, 7232.
61 N. Sakai, H. Kishimoto, K. Yamaji, T. Horita, M. E. Brito and H. Yokokawa, *J. Electrochem. Soc.*, 2007, **154**, B1331.
62 P.-L. Chen and I. W. Chen, *J. Am. Ceram. Soc.*, 1994, **77**, 2289.